1   Regionally strong feedbacks

2   between the atmosphere and terrestrial biosphere

3   Julia K. Green[1]*, Alexandra G. Konings[1,2], Seyed Hamed Alemohammad[1,3], Joseph Berry[4],

4   Dara Entekhabi[3,5], Jana Kolassa[6,7], Jung-Eun Lee[8], Pierre Gentine[1,9]

---

[1] Department of Earth and Environmental Engineering, Columbia University, New York, NY.

[2] Department of Earth System Science, Stanford University, Stanford, CA.

[3] Department of Civil and Environmental Engineering, Massachusetts Institute of Technology, Cambridge, MA.

[4] Department of Global Ecology, Carnegie Institution of Washington, Stanford, CA.

[5] Department of Earth, Atmospheric and Planetary Sciences, Massachusetts Institute of Technology, Cambridge, MA.

[6] University Space Research Association, Columbia, MD.

[7] Global Modeling and Assimilation Office, NASA Goddard Space Flight Center, Greenbelt, MD.

[8] Department of Earth, Environment and Planetary Sciences, Brown University, Providence, RI.

[9] The Earth Institute, Columbia University, New York, NY.

*Correspondence to: jg3405@columbia.edu.

5   **The terrestrial biosphere and atmosphere interact through a series of feedback**

6   **loops. Variability in terrestrial vegetation growth and phenology can modulate fluxes of**

7   **water and energy to the atmosphere, and thus affect the climatic conditions that in turn**

8   **regulate vegetation dynamics. Here we analyze satellite observations of solar-induced**

9   **fluorescence, precipitation, and radiation using a multivariate statistical technique. We**

10   **find that biosphere-atmosphere feedbacks are globally widespread and regionally**

11   **strong: they explain up to 30% of precipitation and surface radiation variance.**

12   **Substantial biosphere-precipitation feedbacks are often found in regions that are**

13   **transitional between energy and water limitation, such as semi-arid or monsoonal**

14   **regions. Substantial biosphere-radiation feedbacks are often present in several**

15   **moderately wet regions and in the Mediterranean, where precipitation and radiation**

16   **increase vegetation growth. Enhancement of latent and sensible heat transfer from**

17   **vegetation accompanies this growth, which increases boundary layer height and**

18   **convection, affecting cloudiness, and consequently incident surface radiation. Enhanced**

19   **evapotranspiration can increase moist convection, leading to increased precipitation.**

20   **Earth system models underestimate these precipitation and radiation feedbacks mainly**

21   **because they underestimate the biosphere response to radiation and water availability.**

22   **We conclude that biosphere-atmosphere feedbacks cluster in specific climatic regions**

23   **that help determine the net CO_2 balance of the biosphere.**

24   By influencing the partitioning of turbulent fluxes at the surface[1], soil moisture and

25   temperature can affect climatic variability[2]. Biospheric variability, in terms of both

26   phenology and stomatal regulation, also strongly modulates turbulent fluxes of both water

27   and energy[3]. Since biospheric variability is regulated by vegetation phenology and root zone

28   soil moisture, it exhibits longer (e.g. multi-month) memory compared to the more commonly

29   studied surface soil moisture and temperature state. Therefore, an understanding of

30   biosphere-atmosphere interactions has the potential to improve seasonal to interannual

31   climatic predictions[4,5,6], and improve predictions of vegetation resilience to climate

32   anomalies[7]. However, global variations in the strength of biosphere-atmosphere feedbacks

33   remain unknown, in part because of the difficulty of observing biospheric fluxes[8].

34   Recent advancements in space-borne observations of solar-induced fluorescence (SIF)

35   have enabled for the first-time a global proxy for gross primary productivity (GPP) and

36   vegetation phenology. SIF is a by-product of photosynthesis[9] related to light-use efficiency

37   (LUE) and to the fraction of absorbed photosynthetic active radiation (fAPAR)[10]. On a

38   canopy or regional scale and at a monthly resolution it is nearly proportional to GPP across

39   various ecosystems. This large-scale correspondence is strongly related to the changes in

40   canopy structure and phenology on absorbed photosynthetic active radiation, in addition to

41   the more subtle changes in LUE[11,12,13,14]. SIF is also generally highly correlated with

42   evapotranspiration (ET)[15] (Supplementary Fig. 1) and correlates with vegetation-driven

43   changes in surface albedo. Here, we use SIF as an integrated measure of vegetation

44   variability, capturing both growth and changes in photosynthetic capacity (Methods).

45   Previous studies of land-atmosphere interactions have typically relied on correlations

46   between land and atmospheric variables[16,17,18]. However, these variables seasonally coevolve,

47   and thus it is difficult to determine whether one variable is causally forcing the other, or if the

48   two are both driven by separate factors[19,20]. Here, these shortcomings are overcome by

49   employing a Multivariate Conditional Granger causality (MVGC) statistical technique using

50   vector autoregressive models (VARs)[21]. This method determines both the strength of the

51   predictive mechanism between variables and the time scale over which these links occur

52   (Methods).

MVGC observational data forcings

54   We apply the MVGC VAR statistical technique to eight years of monthly SIF

55   measurements from the Global Ozone Monitoring Experiment 2 (GOME-2) sensor[22]. SIF-

56   precipitation interactions are assessed using remote sensing-based estimates from the Global

57   Precipitation Climatology Project (GPCP)[23] and SIF-radiation interactions are assessed using

58   photosynthetic active radiation (PAR) from Clouds and the Earth's Radiant Energy System

59   (CERES)[24]. We also use surface air temperature reanalysis data from ERA-Interim[25], as

60   temperature can independently impact and interact with photosynthetic activity[18]. SIF data is

61   relatively noisy, and thus spatial averaging is used to smooth it prior to analysis (Methods). It

62   should be acknowledged that the smoothing could distort results in highly heterogeneous

63   regions where signals from various biomes may be aggregated. Note that, although the linear

64   scaling factor between monthly SIF and GPP varies between ecosystems and climates[12] the

65   pixel-by-pixel data normalization used here removes the geographical variations of this factor

66   (Methods). The analysis presented here is independent of the scaling factor.

67   To identify biosphere-atmosphere coupled feedbacks, we first examine their

68   directional sub-components, i.e. the *atmospheric forcing* (atmosphere ➔ biosphere), as

69   assessed by the response of SIF (GPP) to atmospheric drivers (the fraction of variance in SIF

70   explained by precipitation and PAR), and the *biospheric forcing* (biosphere ➔ atmosphere),

71   as assessed by precipitation and PAR response to SIF (the fraction of variance in

72   precipitation and PAR explained by SIF) (Fig. 1). An F-test with a null-hypothesis of 0-

73   Granger causality (G-causality) (p-value <0.1) is used. The total feedback strength is then

74   defined as the product of these two directional components (Fig. 2). The sign of the feedback

75   is defined as the sign of the first order coefficient of the VAR model from the G-causality

76   analysis. To ensure the results presented here are robust and independent of the seasonal

77   cycle (i.e. due to land-atmosphere interactions), a bootstrap test that conserves the seasonal

78   cycle but breaks the causality by shuffling months from different years is used

79   (Supplementary Fig. 2) and clearly destroys the feedback.

80   Globally, precipitation positively explains the highest fraction of biosphere (SIF)

81   variability in regions that are transitional between wet and dry climates, e.g. semi-arid or

82   monsoonal (Fig. 1a), consistent with previous studies[7,16]. Many of these regions also have

83   high fractions of C4 plants[26], which have higher water use efficiency than C3 species[27], and

84   are therefore expected to be more sensitive to water limitations. The impact of the biosphere

85   on precipitation (Fig. 1b), as assessed by the G-causality of SIF on precipitation, is seen in

86   seasonally dry regions where increases in GPP, in response to increased soil moisture and

87   vegetation growth, is linked with higher latent heat flux and reduced sensible heat flux

88   (Supplementary Fig. 1). Although the impact of SIF on precipitation is less widespread than

89   that of precipitation on SIF, it is significant in many of the same regions. The feedbacks are

90   almost always positive because the monthly positive effect of evapotranspiration on moist

91   convection dominates negative feedback pathways induced by mesoscale surface

92   heterogeneity[28] and the effects of changing albedo. The time scales involved in the feedback

93   mechanisms can vary between regions. The subseasonal signal may represent variability due

94   to early greening induced by increased water supply or to browning induced by water stress,

95   while seasonal and interannual signals may indicate changes in vegetation growth regulated

96   by water availability during cell division. The strongest signals are detected subseasonally in

97   monsoonal Australia, seasonally in Eastern Asia, and both seasonally and interannually in the

98   Sahel and Southern African Monsoonal regions (Supplementary Fig. 3). The dominance of

99   seasonal and interannual time scales in the Sahel, related to biomass variability, is consistent

100   with previous understanding[6,29].

101   PAR has the greatest impact on biosphere fluxes (Fig. 1c) in regions where

102   photosynthesis and vegetation growth is energy limited such as the high latitudes, humid

103   regions of the Eastern US, parts of the Mediterranean, and tropical rainforest regions[30,31].

104   This agrees with the findings of previous studies showing that net primary production (NPP)

105   in these regions is driven by radiation[18]. The biosphere exerts control on PAR in the Eastern

106   US, central Eurasia, African deciduous woodlands as well as in the European Mediterranean

107   region (Fig. 1d). In these very dry or very wet regions, ecosystems rarely enter the

108   transitional regime where stomatal closure depends on soil moisture, and increases in SIF are

109   accompanied by increases in both sensible and latent heat (Supplementary Fig. 1)[32]. The

110   increased sensible heat flux leads to a deeper boundary layer and reduced cloud cover

111   (Supplementary Fig. 4), therefore increasing PAR (Fig. 1d). In the Eastern US, the increase in

112   PAR is mostly attributed to a reduction of low- and mid-level (i.e. congestus) cumulus

113   clouds, typical of summer conditions in this humid climate (Supplementary Fig. 4). By

114   contrast, in the European Mediterranean, PAR is most sensitive to mid- and high-level

115   clouds. In central Eurasia all cloud cover levels negatively impact surface PAR but high-level

116   clouds are the primary reason for the PAR change. The strongest feedbacks between SIF and

117   PAR tend to be on a seasonal scale indicating an increase in ecosystem-scale photosynthetic

118   capacity due to vegetation growth, with exceptions in Madagascar, Australia and central

119   Eurasia where subseasonal and interannual feedbacks dominate (Supplementary Fig. 3). In all

120   PAR feedback regions, PAR is also negatively correlated with precipitation (Supplementary

121   Fig. 4). We note that the European Mediterranean has been highlighted as a hotspot of land-

122   atmosphere coupling in an earlier modeling study, emphasizing the strong coupling between

123   surface turbulent fluxes and the boundary layer response in the region[33]. While a similar

124   coupling mechanism may occur in other regions, they do not exhibit a strong response

125   because other processes (e.g. topography, different land-ocean circulation…) overshadow the

126   regional impact of the biosphere there.

127 **MVGC observational data coupled feedbacks**

128   The results of the *atmospheric* and *biospheric forcings* (Fig. 1) are combined to

129 determine the total variance explained in the coupled biosphere-atmosphere system (Fig. 2

130 and Supplementary Fig. 5). Hotspot regions for the precipitation ➔ SIF ➔ precipitation

131 feedback (Fig. 2a) - which can explain up to 20-30% of the observed precipitation variance -

132 are concentrated in grasslands and savannas (transitional zones) such as monsoonal regions in

133 the Sahel, Eastern India and Northern Australia, as well as the African savanna, Madagascar

134 and the Brazilian savannas. There are other monsoonal regions that despite large shifts in

135 rainfall during the year are not hotspots either due to a lack of ET response to precipitation[34],

136 or a lack of precipitation response to changes in ET[35]. An example of this is the Central Great

137 Plains in North America (a hotspot per previous modeling-based studies of soil moisture-

138 atmosphere interactions[36]), where soil moisture has been shown to have a weak triggering

139 effect on precipitation[20,37]. Indeed, summertime precipitation in this area is dominated by

140 eastward propagating mesoscale convective systems mostly independent of the land

141 surface[38].

142   The PAR ➔ SIF ➔ PAR feedback (Fig. 2b) has hotspots (20-30% of explained

143 variance) in the humid Eastern United States, Southern Brazil, as well as in the

144 Mediterranean basin in Europe. By contrast, in the tropical rainforest regions of Africa and

145 South America there is little response detected for the full feedback loops with either

146 precipitation or PAR (Fig. 2 and Supplementary Fig. 5) suggesting that other factors (such as

147 ecosystem characteristics[39]) dominate the variability of the biosphere there.

148   Although feedbacks between the biosphere and atmosphere are detected in almost all

149 regions, several 'hotspot families' stand out: 1) regions that are either semi-arid or monsoonal

150 for the precipitation feedback and 2) humid regions (the Eastern US) and the Mediterranean

151   for the PAR feedback. No regions exhibit both feedback pathways; one always dominates the

152   other when it is present.

153   **MVGC ESM analysis**

154   The distribution of feedbacks in the observational record is next used to assess Earth

155   System Models (ESMs) (Supplementary Table 1). The distributions of feedback strengths for

156   model and observational results (Fig. 3) summarize the differences between the biosphere-

157   atmosphere feedback detected by each CMIP5 model (Supplementary Figs 6, 7 and 8) and

158   the observational record. In the model analysis, GPP is used as a proxy for the biosphere in

159   lieu of SIF. Our results are normalized in terms of explained variance for each pixel so that

160   the proportionality factor of SIF and GPP does not impact the pixel-wise metric results. To

161   increase robustness, 50 years of data are used for the model analysis (1956-2005) rather than

162   the shorter period we are constrained by for the observational analysis[40].

163   The median of all ESMs fall below the first quartile of the observational data results

164   for the precipitation ➔ biosphere ➔ precipitation feedback (Fig. 3a). Models significantly

165   underestimate the magnitude and the range of both the *atmospheric* and *biospheric forcings*

166   (except for CMCC-CESM) (Supplementary Fig. 6), although underestimation is more severe

167   in the case of the precipitation ➔ biosphere component. The observational PAR ➔ biosphere

168   ➔ PAR feedback strength (Fig. 3b) also has a higher median value than that of the ESMs.

169   Both the precipitation and PAR *atmospheric forcings* are underestimated because of

170   photosynthesis misrepresentation in ESMs (Supplementary Fig. 6)[41]. Despite some spatial

171   similarities between modeled feedbacks and observational results (Supplementary Figs 7 and

172   8), models systematically underestimate the impact of the biosphere on precipitation, and

173   noticeably miss the variance explained by observations in monsoonal Australia. On the other

174   hand, the modeled impact of the biosphere on PAR varies drastically between models and can

175 be either over- or under-estimated (Supplementary Fig. 6). These inter-model discrepancies

176 are likely due to the misrepresentation of convection in models, and the challenges of

177 correctly representing it over land regions[42,43]. Interestingly, in general, ESM errors in

178 representing the atmospheric forcing on the biosphere are even more severe than errors in

179 representing the biospheric forcing on the atmosphere. This suggests that better

180 representations of photosynthesis and water stress sensitivities would have a larger impact on

181 improving the ESM representation of biosphere-atmosphere feedbacks, than improved

182 convection representation.

183   This study provides the first causal observational diagnostic of biosphere-atmosphere

184 feedbacks on subseasonal to interannual time scales. These feedbacks are strong in semi-arid

185 and monsoonal regions, which are key in determining whether the yearly global terrestrial

186 biosphere acts as a net CO_2 source or sink[7,16]. As such biosphere-atmosphere feedbacks

187 regulate interannual hydrology and climate in these regions as well as the global carbon

188 cycle. Additionally, due to the high percentages of atmospheric variability explained by

189 vegetation processes, subseasonal and seasonal climate predictions can greatly benefit from

190 better vegetation characterization in ESMs. In turn this will improve subseasonal to seasonal

191 climate and hydrologic forecasts, which are crucial for optimizing management decisions

192 pertaining to food security, water supplies, and disaster management such as droughts and

193 heat waves.

Main Text References

195   1.   Bateni, S. M. & Entekhabi, D. Relative efficiency of land surface energy balance

196   components. *Water Resour. Res.* **48,** 1–8 (2012).

197   2.   Koster, R. D., Suarez, M. J. & Heiser, M. Variance and Predictability of Precipitation

198   at Seasonal-to-Interannual Timescales. *J. Hydrometeorol.* **1,** 26–46 (2000).

199   3.   van den Hurk, B. J. J. M., Viterbo, P. & Los, S. O. Impact of leaf area index

200   seasonality on the annual land surface evaporation in a global circulation model. *J.*

201   *Geophys. Res.* **108,** 5.1-5.7 (2003).

202   4.   Guo, Z., Dirmeyer, P. A., Delsole, T. & Koster, R. D. Rebound in atmospheric

203   predictability and the role of the land surface. *J. Clim.* **25,** 4744–4749 (2012).

204   5.   Koster, R. D. *et al.* The Second Phase of the Global Land–Atmosphere Coupling

205   Experiment: Soil Moisture Contributions to Subseasonal Forecast Skill. *J.*

206   *Hydrometeorol.* **12,** 805–822 (2011).

207   6.   Zeng, N., Neelin, J., Lau, K. & Tucker, C. Enhancement of Interdecadal Climate

208   Variability in the Sahel by Vegetation Interaction. *Science* **286,** 1537–1540 (1999).

209   7.   Poulter, B. *et al.* Contribution of semi-arid ecosystems to interannual variability of the

210   global carbon cycle. *Nature* **509,** 600–603 (2014).

211   8.   Koster, R. D. *et al.* On the nature of soil moisture in land surface models. *J. Clim.* **22,**

212   4322–4335 (2009).

213   9.   Porcar-Castell, A. *et al.* Linking chlorophyll a fluorescence to photosynthesis for

214   remote sensing applications: Mechanisms and challenges. *J. Exp. Bot.* **65,** 4065–4095

215   (2014).

216   10.   Guanter, L. *et al.* Global and time-resolved monitoring of crop photosynthesis with

217   chlorophyll fluorescence. *Proc. Natl. Acad. Sci. U. S. A.* **111,** E1327-33 (2014).

218   11.   Zhang, Y. *et al.* Remote Sensing of Environment Consistency between sun-induced

219   chlorophyll fluorescence and gross primary production of vegetation in North

220   America. *Remote Sens. Environ.* **183,** 154–169 (2016).

221   12.   Frankenberg, C. *et al.* New global observations of the terrestrial carbon cycle from

222   GOSAT: Patterns of plant fluorescence with gross primary productivity. *Geophys. Res.*

223   *Lett.* **38,** L17706 (2011).

224   13.   Frankenberg, C., O'Dell, C., Guanter, L. & McDuffie, J. Remote sensing of near-

225   infrared chlorophyll fluorescence from space in scattering atmospheres: Implications

226   for its retrieval and interferences with atmospheric CO_2 retrievals. *Atmos. Meas.*

227   *Tech.* **5,** 2081–2094 (2012).

228   14.   Wood, J. D. *et al.* Multi-scale analyses reveal robust relationships between gross

229   primary production and solar induced fluorescence. *Geophys. Res. Lett.* **In Review:,**

230   533–541 (2016).

231   15.   Schlesinger, W. H. & Jasechko, S. Transpiration in the global water cycle. *Agric. For.*

232   *Meteorol.* **189–190,** 115–117 (2014).

233   16.   Ahlström, A. *et al.* The dominant role of semi-arid ecosystems in the trend and

234   variability of the land CO2 sink. *Science (80-.).* **348,** 895–899 (2015).

235   17.   Beer, C. *et al.* Terrestrial gross carbon dioxide uptake: global distribution and

236   covariation with climate. *Science* **329,** 834–838 (2010).

237   18.   Nemani, R. R. *et al.* Climate-driven increases in global terrestrial net primary

238   production from 1982 to 1999. *Science* **300,** 1560–1563 (2003).

239   19.   Sugihara, G. *et al.* Detecting causality in complex ecosystems. *Science* **338,** 496–500

240   (2012).

241   20.   Tuttle, S. & Salvucci, G. Empirical evidence of contrasting soil moisture–precipitation

242   feedbacks across the United States. **352,** 825–828 (2016).

243   21.   Barnett, L. & Seth, A. K. The MVGC multivariate Granger causality toolbox: A new

244   approach to Granger-causal inference. *J. Neurosci. Methods* **223,** 50–68 (2014).

245   22.   Joiner, J. *et al.* Global monitoring of terrestrial chlorophyll fluorescence from

246   moderate spectral resolution near-infrared satellite measurements: methodology,

247   simulations, and application to GOME-2. *Atmos. Meas. Tech. Discuss.* **6,** 3883–3930

248   (2013).

249   23.   Pendergrass, A. & N. C. for A. R. S. (Eds). The Climate Data Guide: GPCP

250   (Monthly): Global Precipitation Climatology Project. 1–2 (2016). Available at:

251   https://climatedataguide.ucar.edu/climate-data/gpcp-monthly-global-precipitation-

252   climatology-project.

253   24.   Wielicki, B. A. *et al.* Clouds and the Earth's Radiant Energy System (CERES): An

254   Earth Observing System Experiment. *Bull. Amer. Meteor. Soc.* **77,** 853–868 (1996).

255   25.   Dee, D. P. *et al.* The ERA-Interim reanalysis: Configuration and performance of the

256   data assimilation system. *Q. J. R. Meteorol. Soc.* **137,** 553–597 (2011).

257   26.   Still, C. J., Berry, J. A., Collatz, G. J. & DeFries, R. S. Global distribution of C 3 and

258   C 4 vegetation: Carbon cycle implications. *Global Biogeochem. Cycles* **17,** 6-1-6–14

259   (2003).

260   27.   Ghannoum, O. C4 photosynthesis and water stress. *Ann. Bot.* **103,** 635–644 (2009).

261   28.   Guillod, Benoit P. (Institute for Atmospheric and Climate Science, Department of

262   Environmental Systems Science, E. Z., Orlowsky, B., Miralles, D. G., Teuling, A. J. &

263   Seneviratne, S. I. Reconciling spatial and temporal soil moisture effects on afternoon

264   rainfall. *Nat. Commun.* **6,** 6443 (2015).

265   29.   Charney, J. G. Dynamics of deserts and drought in the Sahel. *Q. J. R. Meteorol. Soc.*

266   **101,** 193–202 (1975).

267   30.   Anber, U., Gentine, P., Wang, S. & Sobel, A. H. Fog and rain in the Amazon. *Proc.*

268   *Natl. Acad. Sci.* **112,** 11473–11477 (2015).

269   31.   Brando, P. M. *et al.* Seasonal and interannual variability of climate and vegetation

270   indices across the Amazon. *Proc. Natl. Acad. Sci. U. S. A.* **107,** 14685–90 (2010).

271   32.   Seneviratne, S. I. *et al.* Investigating soil moisture-climate interactions in a changing

272   climate: A review. *Earth-Science Rev.* **99,** 125–161 (2010).

273   33.   Seneviratne, S. I., Lüthi, D., Litschi, M. & Schär, C. Land-atmosphere coupling and

274   climate change in Europe. *Nature* **443,** 205–209 (2006).

275   34.   Dirmeyer, P. A. The terrestrial segment of soil moisture-climate coupling. *Geophys.*

276   *Res. Lett.* **38,** L16702 (2011).

277   35.   Koster, R. D. & Suarez, M. J. Impact of Land Surface Initialization on Seasonal

278   Precipitation and Temperature Prediction. *J. Hydrometeorol.* **4,** 408–423 (2003).

279   36.   Koster, R. D. *et al.* GLACE: The Global Land – Atmosphere Coupling Experiment.

280   Part I: Overview. *J. Hydrometeorol.* **7,** 611–625 (2006).

281   37.   Findell, K. L., Gentine, P., Lintner, B. R. & Kerr, C. Probability of afternoon

282   precipitation in eastern United States and Mexico enhanced by high evaporation. *Nat.*

283   *Geosci.* **4,** 434–439 (2011).

284   38.   Storer, R. L., Zhang, G. J. & Song, X. Effects of convective microphysics

285   parameterization on large-scale cloud hydrological cycle and radiative budget in

286   tropical and midlatitude convective regions. *J. Clim.* **28,** 9277–9297 (2015).

287   39. Levine, N. M. *et al.* Ecosystem heterogeneity determines the ecological resilience of

288   the Amazon to climate change. *Proc. Natl. Acad. Sci.* (2015).

289   doi:10.1073/pnas.1511344112

290   40. Findell, K. L., Gentine, P., Lintner, B. R. & Guillod, B. P. Data Length Requirements

291   for Observational Estimates of Land–Atmosphere Coupling Strength. *J.*

292   *Hydrometeorol.* **16,** 1615–1635 (2015).

293   41. Zhou, S., Duursma, R. A., Medlyn, B. E., Kelly, J. W. G. & Prentice, I. C. How should

294   we model plant responses to drought? An analysis of stomatal and non-stomatal

295   responses to water stress. *Agric. For. Meteorol.* **182–183,** 204–214 (2013).

296   42. Bony, S. *et al.* Clouds, circulation and climate sensitivity. *Nat. Geosci.* **8,** 261–268

297   (2015).

298   43. Zhao, M. *et al.* Uncertainty in model climate sensitivity traced to representations of

299   cumulus precipitation microphysics. *J. Clim.* **29,** 543–560 (2016).

300

301 **Corresponding author**

302   Correspondence and requests for materials should be addressed to JKG

303 (jg3405@columbia.edu).

315 **Author Contributions**

316   JKG, AGK and PG wrote the main manuscript text. JKG, PG and SHA prepared

317 figures. SHA processed the CMIP5 simulations. JKG, PG and AGK designed the study. All

318 authors reviewed and edited the manuscript.

Figure Captions

Figure 1. *Atmospheric forcings* **and** *biospheric forcings*. X ➜ Y represents the fraction of variance of Y explained by X, for the *atmospheric forcing* (atmosphere ➜ biosphere) (**a,c**), and *biospheric forcing* (biosphere ➜ atmosphere) (**b,d**). The signs of the fractions in the top row show whether the atmospheric variable increases (positive) or decreases (negative) the biosphere flux, while in the bottom row they show whether the biosphere increases or decreases the atmospheric response. Oceans and regions where SIF partial correlations are less than 0.1 are shown in white. Pixels without significance are shown in gray (p-value<0.1).

Fig. 2. **Hotspots of terrestrial biosphere-atmosphere feedbacks**. The fraction of biosphere-atmosphere coupling variance explained for the full feedback loop: precipitation ➜ SIF ➜ precipitation (**a**) and PAR ➜ SIF ➜ PAR (**b**). The sign of the fraction shows whether the feedback is positive or negative. Oceans and regions where SIF partial correlations are less than 0.1 are shown in white. Pixels without significance are shown in gray (p-value<0.1).

Fig. 3. Comparison of observational and Earth System Model results. Boxplots showing the distributions of significant observational and model results for the fractions of variance explained for the feedbacks of precipitation ➜ biosphere ➜ precipitation (**a**) and PAR ➜ biosphere ➜ PAR (**b**). Boxes are defined by the upper quartile, median and lower quartile of the data while whiskers are defined by the outliers. Only significant pixels are represented (p-value<0.1).

Methods

Datasets

Observational remote sensing data is used for SIF, precipitation, and PAR, while quasi-observational reanalysis data is used for temperature. GOME-2, version 2.6[22] (overpass time of 9:30am) is used for SIF, precipitation data is obtained from version 1.2 of GPCP[23], PAR from CERES[24], and surface air temperature (1000mb) data from ERA-Interim[25] (see Data availability). While a longer observational data record would allow further insight into interannual variability, we are limited by the satellite data record availability.

There is a certain amount of uncertainty inherent to each product that is described in detail in their data quality summaries. The SIF data is especially noisy (particularly in South America where there are less frequent measurements due to clouds, specifically in the rainforest, and noise from the South Atlantic Anomaly)[22]. Thus, in addition to a standard normalization (described below), SIF data is averaged with the 8 adjacent pixels surrounding the pixel of interest to smooth the remaining noise. On rare pixels, we note that SIF appears to cause an increase in both precipitation and PAR (Figs 1b and d) but this effect is attributed to the use of nine-pixels spatially smoothing of the SIF signal.

The monthly SIF data is calculated from daily measurements (level 2) when the effective cloud fraction is <30%. It should be noted that effective cloud fraction is not equivalent to geometric cloud fraction but is instead based on a Lambertian model that considers cloud reflectance and albedo[44,45,46]. It has been demonstrated that in a typical pixel with a true cloud fraction of 40% that over 80% of the SIF signal can still be retrieved for very thick cloud optical thicknesses (up to 10)[47]. The effective cloud fraction is typically lower than the geometric one.

369   While cloud filtering could result in a slight bias, it has been shown that altering the

370   effective cloud fraction threshold between 0 and 50 percent only minimally affects the spatial

371   and temporal patterns of SIF[22]. Therefore, we expect minimal bias due to the filtering at the

372   monthly resolution that we consider in our analysis. The one region where the cloud coverage

373   filtering may reduce G-causality detected is in the wet tropics where there is a higher

374   prevalence of clouds. It is possible that the PAR ➔ SIF ➔ PAR feedbacks might be

375   underestimated in this region because of the cloud contamination.

376   **SIF-GPP relationship**

377   This study uses SIF as a proxy for GPP. SIF is mechanistically linked to GPP[9,48],

378   through both light use efficiency and fAPAR[49], and has been shown to have a near-linear

379   relationship with GPP at both canopy and ecosystem scales[11,12,50,51,46,52]. While the hourly

380   leaf-level relationship between SIF and GPP has been estimated as curvilinear (SIF continues

381   to increase after the maximum rate of photosynthesis has been reached)[11], the relationship at

382   larger and longer time scales (e.g., monthly) becomes linear likely due to the effects of

383   averaging across a canopy of leaves representing varying light conditions[11].

384   The linearity between SIF and GPP has been observed across biomes using a variety

385   of datasets, including flux tower validation[46,52]. As is shown in Supplementary Fig. 1, SIF

386   correlates strongly with monthly global GPP estimates from Fluxnet-MTE in regions outside

387   of the wet tropics. The SIF-GPP correlation is lower in the wet tropics as the machine

388   learning upscaling approach of the Fluxnet-MTE GPP product has the greatest uncertainty in

389   these regions, as there are few(er) eddy covariance towers there that are used for training[53,54].

390   Additionally, tropical forest GPP exhibits minimal seasonality[55], and thus the lower

391   correlation can be attributed to the fitting of noise (R^2 by construction will be small). It has

392   nonetheless been shown that the minimal seasonality in SIF observed in the Amazon

393   correctly corresponds to the seasonality of carbon dioxide[56] and MODIS near-infrared

394   reflectance related to photosynthesis[55]. As a result, SIF has been used as a proxy for GPP

395   interannual variability[11].

396   The linear scaling factor between SIF and GPP varies spatially. Yet, when we

397   normalize the data prior to running the G-Causality, the differing slope values should not

398   impact results since we look at each pixel (location/ecosystem) separately.

399   **Conditional MVGC**

400   We base our analysis on Multivariate Granger causality, using a MVGC MATLAB

401   toolbox[21], which allows for time and frequency domain MVGC analysis of time series data.

402   The method fits multivariate VAR models to time series. Conditional MVGC compares VAR

403   models with and without (potentially causal) variables. For example, if the addition of past

404   values of precipitation improves the quality of the VAR model prediction for SIF (that uses

405   the autoregressive histories of other variables: SIF, PAR and temperature), then precipitation

406   is considered to have a G-causal influence[57]. If there is no significant information gained

407   (based on an F-test with a null-hypothesis of no G-causality), then the variables are

408   considered not to have a causal link.

409   Prior to applying the MVGC technique, the data obtained are aggregated to 1-degree

410   by 1-degree monthly data. Monthly data are used to reduce random noise in the original SIF

411   daily data and to achieve consistency with the monthly-aggregated resolution of Coupled

412   Model Intercomparison Project Phase 5 (CMIP5) model data. For each dataset, the long-term

413   mean value is subtracted from each pixel and it is normalized by its long-term standard

414   deviation. After normalization, SIF data is averaged with the 8 adjacent pixels surrounding

415   the pixel of interest to smooth the remaining noise inherent in the SIF data from GOME-2.

416   Single missing monthly values (approximately 4% of the pixels per month) are interpolated

417   using temporal splines. Prior to performing the normalization and running the MVGC

418   analysis, partial correlations are calculated between non-normalized SIF and atmospheric

419   variables, and if the absolute correlation falls below a value of 0.1, the atmospheric variable

420   is considered non-significant for that pixel and is not included in the analysis. Although

421   results of the analysis are not shown for surface air temperature (temperature at 1000mb), it is

422   used in the analysis, to account for its influence when determining the feedbacks involving

423   precipitation, PAR and SIF. For example, by including temperature in the analysis we

424   guarantee that the G-causality between PAR and SIF is not instead a reflection of the effects

425   of temperature (or related to vapor pressure deficit), which can be correlated with PAR. For

426   all analyses, we use a conservative p-value calculation given the high auto-correlation in the

427   variables of interest, which reduces the degrees of freedom in the number of samples.

428   Note that we intentionally do not remove the seasonal cycle in pre-processing. Small

429   stochastic amplitude and phase modulations of the seasonality (e.g. large monthly cloud

430   cover or colder than usual temperatures in a particular year) induce non-additive widening of

431   the amplitude and phase spectra so that subtracting the climatology artificially reduces

432   specific frequencies and phases, potentially removing part of the causal signal. This risk is

433   amplified by the relatively short remote sensing record used, which could lead to an

434   imperfect definition of the climatological seasonal cycle. Indeed, where the seasonal signal

435   amplitude and phase have a causal effect we want to capture this (such as the rainfall impact

436   on vegetation green-up and SIF in monsoonal regions). Because the VAR models can capture

437   seasonal periodicity, the MVGC analysis is not affected by the risk of false attribution of

438   causality due to simple lagged seasonality, as is further demonstrates in the examples below.

439   After normalization of the data and checking that partial correlations between SIF and

440   the other variables fall above 0.1, the Akaike information criterion is calculated and defines

441   the best model order up to the maximum model order, specified as 6 months

442   ('tsdata_to_infocrit.m' function in the MVGC MATLAB toolbox). The best actual model

443   order used displays the memory of the biosphere-atmosphere interactions (Supplementary

444   Fig. 9): model orders of 1 correspond to regions where memory in the system is short and

445   causal influence between the atmosphere and biosphere is weak. Using the calculated model

446   order, an ordinary least-square regression is used to determine the multivariate-VAR model

447   coefficients ('tsdata_to_var.m'). The autocovariance function is created

448   ('var_to_autocov.m'), and from this we calculate the time domain pair-wise conditional

449   causalities ('autocov_to_pwcgc.m'). To test time-domain significance, we calculate the p-

450   values, which are compared to our chosen p-value of less than 0.1 ('mvgc_pval.m'). An F-

451   test with a null-hypothesis of no G-causality is used and only significant pixels are displayed

452   in figures. To perform the analysis in the frequency domain and identify subseasonal (<3

453   months), seasonal (3 to 12 months) and interannual (>1 year) feedbacks, we calculate the

454   spectral-conditional G-causality ('autocov_to_spwcgc.m') (Supplementary Fig. 3).

455   We check that the G-causality in the frequency domain integrates to the time domain

456   by integrating the frequency results ('smvgc_to_mvgc.m') and then subtracting the output

457   from the time domain result. Checks are performed throughout the process so that the

458   analysis is automatically exited should there be a failed calculation.

459   A sample first order VAR model to explain the variability of SIF is displayed in

460   equation 1 with A, P, T and sig representing the VAR coefficient matrix, precipitation,

461   temperature, and significance (1 for significant, 0 for insignificant at $p < 0.1$) accordingly.

$$SIF(t) = A_{(SIF)}\, SIF_{(t-1)} + A_{(P\ on\ SIF)}\, P_{(t-1)}\, sig_{(P\ on\ SIF)} \tag{1}$$

$$+ A_{(PAR\ on\ SIF)}\, PAR_{(t-1)}\, sig_{(PAR\ on\ SIF)}$$

$$+ A_{(T\ on\ SIF)}\, T_{(t-1)}\, sig_{(T\ on\ SIF)} + \varepsilon$$

462   With the addition of the auto-regressive histories of each variable, the VAR model

463   captures the original SIF data more accurately. We acknowledge that other factors not

464   included in this analysis can affect SIF variability (such as naturally and anthropogenically

465   caused disturbances), and is one of the reasons (along with sensor noise) that we cannot

466   predict 100% of the variable variance, even with our full VAR model.

467   **Synthetic Bootstrap Tests**

468   To demonstrate the effectiveness of this method, we perform several additional tests

469   of the conditional MVGC on synthetic data where causal links can be specified. In the first

470   three test scenarios PAR and precipitation (P) time series are assumed to be sinusoidal with

471   amplitude modulation – AM – and frequency modulation – FM –, as well as additive noise

472   (equations 2 and 3). We define two similar test cases except that one has a causal link

473   (equation 4) while the other does not (non-causal) (equation 5). We assume that the noise is

474   normally distributed (and thus have a white noise/flat spectrum in the frequency domain). To

475   test the frequency response, PAR is assumed to have a yearly frequency

476     $\omega = 2\pi / (12 \text{ months})$ (equation 2) while precipitation is assumed to have twice-yearly

477   frequency 2ω (i.e. two wet/dry seasons per year) (equation 3).

$$PAR(t) = 100(1 + 0.25 A_t^{PAR})\sin\left(\left(1 + \frac{1}{24}F_t^{PAR}\right)\omega t - \pi/2\right) + 25\varepsilon_t^{PAR} \tag{2}$$

$$P(t) = 100(1 + 0.25 A_t^{P})\sin\left(\left(1 + \frac{1}{24}F_t^{P}\right)2\omega t - \pi/4\right) + 25\varepsilon_t^{P} \tag{3}$$

478   with A_t^{PAR}, F_t^{PAR}, ϵ_t^{PAR}, A_t^{P}, F_t^{P}, ϵ_t^{P} i.i.d. normally distributed with unit variance $N(0,1)$.

479   In the *causal case*, SIF is defined as a lagged version of precipitation and radiation

480   (with t in months) (equation 4):

$$SIF = 0.2(1+0.25A_t^{SIF})P(t-2)+0.8(1+0.25B_t^{SIF})PAR(t-1)+25\epsilon_t^{SIF} \quad . \tag{4}$$

481   with $A_t^{SIF}, B_t^{SIF}, \epsilon_t^{SIF}$ i.i.d. normally distributed with unit variance $N(0,1)$. We use 50 years of

482   synthetic data and one realization for the test.

483   The conditional G-causality finds that only radiation and precipitation are causing SIF

484   and not the converse (Supplementary Fig. 10). In addition, the magnitude of radiation on SIF

485   is four times stronger than the one of precipitation on SIF, as expected based on the time

486   series generated (equation 4).

487   To emphasize that these results are not spurious, we perform a second, similar test but

488   with a *non-causal* time series (equation 5). This non-casual SIF time series is not induced by

489   PAR nor precipitation. It is statistically similar to the causal scenario, composed of lagged

490   sinusoids with similar frequencies to PAR and precipitation, but without a causal mechanism.

491   For the precipitation and radiation time series we allow for both amplitude and frequency

492   modulations so that both amplitude and phase are stochastic (similar to radiation and

493   precipitation monthly time series).

$$
\begin{aligned}
SIF &= 20(1+0.25a_t^{SIF})\sin\left(\left(1+\frac{1}{24}b_t^{SIF}\right)2\omega t - \pi/2 - (2/12)2\pi\right) \\
&+ \quad 80(1+0.25c_t^{SIF})\sin\left(\left(1+\frac{1}{24}d_t^{SIF}\right)\omega t - \pi/4 - (1/12)2\pi\right) \\
&+ \quad\quad\quad\quad\quad\quad 25e_t^{SIF}
\end{aligned} \quad . \tag{5}
$$

494   The conditional MVGC analysis of this non-causal time series shows no significant G-

495   causality, as expected (Supplementary Fig. 10).

496   In the third test we bootstrap every month of equations 2-4 across years, clearly

497   destroying the causality in the time series (as the same month from another year is used)

498   while preserving the climatology (and seasonal cycle). As seen in Supplementary Figure 10,

499   the test again finds no causality in the time series, further confirming the quality of the

500   method and its applicability for our type of time series.

501   In a fourth and final synthetic data analysis, we test whether we can detect a *causal*

502   full-feedback loop. We repeat the original *causal* test (equation 4), switching the original

503   equation for PAR (equation 2) for one that also includes SIF as a driver (equation 6).

$$PAR = PAR + 0.4\,SIF\,\mathrm{var}(PAR)/\mathrm{var}(SIF). \tag{6}$$

504   As expected, in addition to the causality detected previously in the *causal* test of precipitation

505   and PAR on SIF, we also detect significant causality of SIF on PAR (Supplementary Fig. 10).

Observational Bootstrap Test

507   To further test the assumption that the observed causation of the biosphere on the

508   atmosphere is not an artifact of the seasonal cycle, we perform a bootstrap analysis with 100-

509   realizations at the global scale. Observational data is sampled by randomly swapping the

510   same months across years for each variable: that is the seasonality is preserved while the

511   causal link from month to month is destroyed. As expected, very few pixels showed any G-

512   causality (Supplementary Fig. 2): only 6.2% of the SIF ➔ precipitation results, and 6.9% of

513   the SIF ➔ PAR results were found to be significant at the 95% confidence level (had more

514   than 5/100 realizations per pixel with significant results based on an F-distribution with a p-

515   value < 0.1). The resulting averaged pair-wise conditional G-causality shows almost no

516   signal, with a peak of less than 0.05 compared to 0.3 for the original dataset (Supplementary

517   Fig. 2). In addition, the resulting geographical patterns reflect mostly random noise. This

518   further emphasizes the physical nature of our assessed causation between the biosphere and

519   the atmosphere.

Vector Autoregressive Models

521   The VAR models obtained from the G-causality analysis are used to quantify the

522   fraction of variance in the biosphere explained by the atmosphere and vice versa. We tested

523   for normality and homoscedasticity of the residuals during the VAR fits and excluded pixels

524   that did not meet these criteria (3-6% of pixels depending on the feedback). Using the VAR

525   coefficients generated by the analysis (to account for cross variations), VAR models are

526   created for each atmospheric variable with and without the inclusion of SIF. VAR models are

527   also created for SIF with and without the inclusion of each atmospheric variable. The

528   fractions of observed SIF variance explained by each atmospheric component is computed

529   (equation 7):

$$f_{X \to SIF} = \frac{\mathrm{var}(SIF_{AR \text{ fit with X}}) - \mathrm{var}(SIF_{AR \text{ fit without X}})}{\mathrm{var}(SIF)} \tag{7}$$

530

531   as well as the fraction of each atmospheric variable observed variance explained by SIF

532   (equation 8) (Fig. 1):

$$f_{SIF \to Y} = \frac{\mathrm{var}(Y_{AR \text{ fit with SIF}}) - \mathrm{var}(Y_{AR \text{ fit without SIF}})}{\mathrm{var}(Y)} \tag{8}$$

533   These are combined to obtain the full feedback fractions (equation 9) (Fig. 2 and

534   Supplementary Fig. 5):

$$f_{X \to SI \to Y} = \tag{9}$$

$$\frac{\mathrm{var}(SIF_{AR \text{ fit with X}}) - \mathrm{var}(SIF_{AR \text{ fit without X}})}{\mathrm{var}(SIF)} \times$$

$$\frac{\mathrm{var}(Y_{AR \text{ fit with SIF}}) - \mathrm{var}(Y_{AR \text{ fit without SIF}})}{\mathrm{var}(Y)}$$

535   The feedback is defined as positive or negative by taking the VAR model first order

536   coefficients, which is then compared with the VAR model coefficient with the greatest

537   absolute magnitude as further verification. The leading order coefficient of the AR model

538 could be used in lieu of the first order one but given the rapid decay of the autocorrelation

539 function and the reduced VAR model order (typically less than 2, Supplementary Fig. 9) we

540 use the sign of the first order coefficient. The two estimates of the sign differ in limited

541 regions.

542 **CMIP5 Model Simulations**

543 For the Earth System models from the CMIP5 collection (Supplementary Table 1),

544 the same analysis used for the observational data is applied. Only those models that included

545 GPP data are used. The time period of 1956-2005 is used to obtain statistics that are robust

546 across interannual variability[40]. The true feedback strengths have likely not changed

547 significantly from this earlier, longer time period and the period used for the observational

548 analysis, but we acknowledge that land-use and land-cover changes can affect the feedback

549 metrics (but are also model dependent). One realization of the historical run was used for

550 each model[58].

551 VAR models are created based on coefficients calculated in the MVGC analysis for

552 each ESM, and the fraction of variance explained in biosphere-atmosphere coupling from

553 each variable is calculated using equations 5-7.

554 **Code availability**

555 The code used as the basis for the study can be accessed from

556 http://www.sussex.ac.uk/sackler/mvgc/.

557 **Data availability**

558 All data supporting the findings of this study are freely available from the following

559 locations:

560 • GOME-2 SIF: https://avdc.gsfc.nasa.gov/pub/data/satellite/MetOp/GOME_F/

561   • GPCP precipitation:

562   http://iridl.ldeo.columbia.edu/SOURCES/.NASA/.GPCP/.V1DD/.V1p2/

563   • CERES PAR: https://ceres-tool.larc.nasa.gov/ord-tool/jsp/SYN1degSelection.jsp

564   • CERES cloud coverage:

565   https://ceres-tool.larc.nasa.gov/ord-tool/jsp/ISCCP-D2Selection.jsp

566   • ERA-Interim temperature and boundary layer height:

567   http://apps.ecmwf.int/datasets/data/interim-full-mnth/levtype=sfc/

568   • Fluxnet-MTE surface flux and GPP data:

569   https://www.bgc-jena.mpg.de/geodb/projects/Data.php

570   • CMIP5 model data: https://pcmdi.llnl.gov/

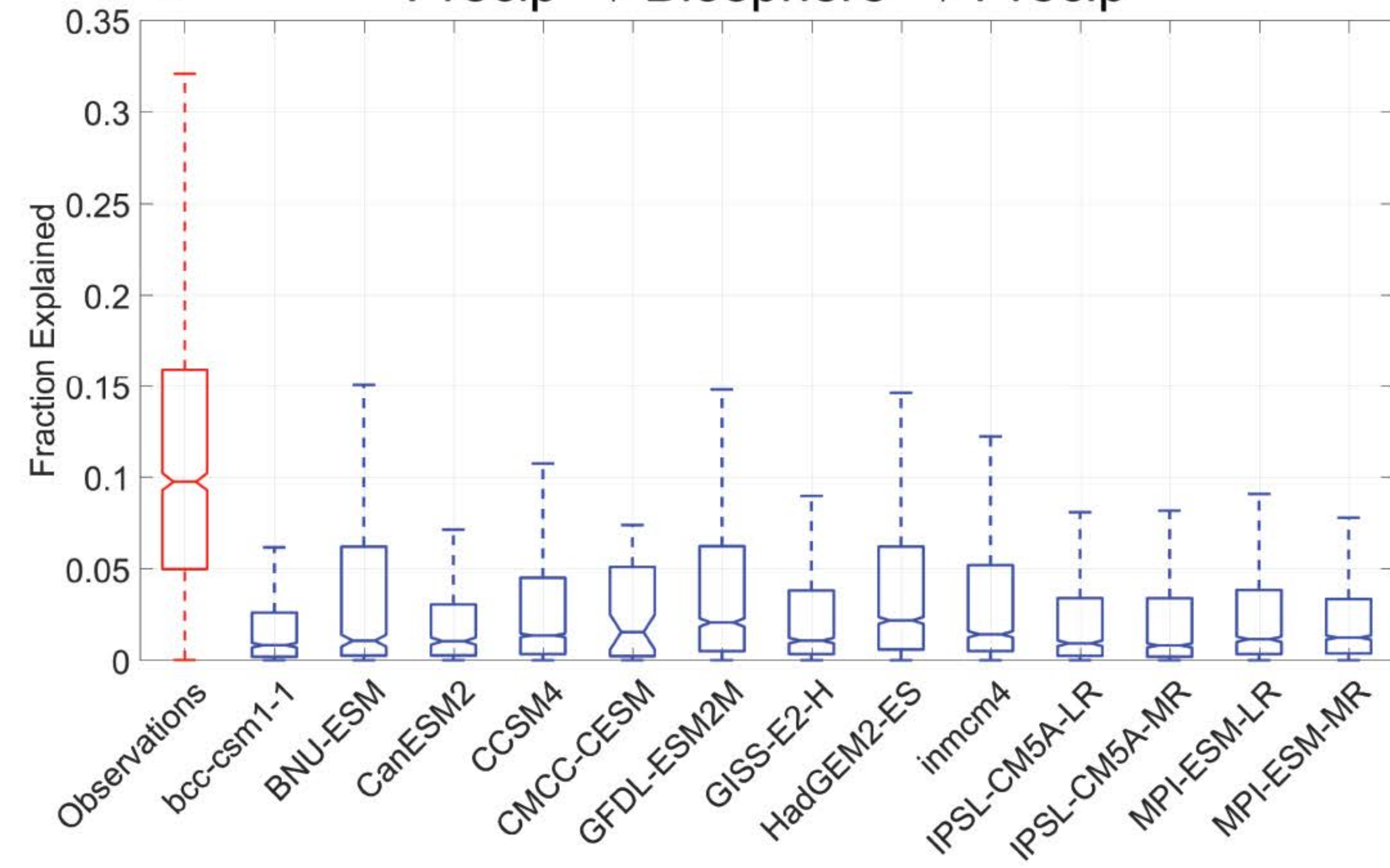571   Additional intermediate datasets produced as part of the study can be made available

572 upon request.

Methods References

44. Koelemeijer, R. B. a., Stammes, P., Hovenier, J. W. & de Haan, J. F. A fast method for retrieval of cloud parameters using oxygen A band measurements from the Global Ozone Monitoring Experiment. *J. Geophys. Res.* **106,** 3475 (2001).

45. Stammes, P. *et al.* Effective cloud fractions from the Ozone Monitoring Instrument: Theoretical framework and validation. *J. Geophys. Res. Atmos.* **113,** 1–12 (2008).

46. Joiner, J. *et al.* The seasonal cycle of satellite chlorophyll fluorescence observations and its relationship to vegetation phenology and ecosystem atmosphere carbon exchange. *Remote Sens. Environ.* **152,** 375–391 (2014).

47. Joiner, J. *et al.* Filling-in of near-infrared solar lines by terrestrial fluorescence and other geophysical effects: Simulations and space-based observations from SCIAMACHY and GOSAT. *Atmos. Meas. Tech.* **5,** 809–829 (2012).

48. Lee, J. *et al.* Forest productivity and water stress in Amazonia : observations from GOSAT chlorophyll fluorescence Forest productivity and water stress in Amazonia : observations from GOSAT chlorophyll fluorescence. *Proc. R. Soc. B* **280,** 20130171 (2013).

49. Duveiller, G. & Cescatti, A. Spatially downscaling sun-induced chlorophyll fluorescence leads to an improved temporal correlation with gross primary productivity. *Remote Sens. Environ.* **182,** 72–89 (2016).

50. Guanter, L. *et al.* Retrieval and global assessment of terrestrial chlorophyll fluorescence from GOSAT space measurements. *Remote Sens. Environ.* **121,** 236–251 (2012).

51. Guanter, L. *et al.* Global and time-resolved monitoring of crop photosynthesis with

596   chlorophyll fluorescence. *Proc. Natl. Acad. Sci. U. S. A.* **111,** E1327-33 (2014).

597 52. Yang, X., Tang, J., Mustard, J. F., Lee, J. & Rossini, M. Solar-induced chlorophyll

598   fluorescence correlates with canopy photosynthesis on diurnal and seasonal scales in a

599   temperate deciduous forest. **42,** 2977–2987 (2015).

600 53. Anav, A. *et al.* Reviews of Geophysics primary production : A review. *Rev. Geophys.*

601   787–818 (2015).

602 54. Jung, M. *et al.* Global patterns of land-atmosphere fluxes of carbon dioxide, latent

603   heat, and sensible heat derived from eddy covariance, satellite, and meteorological

604   observations. *J. Geophys. Res.* **116,** G00J07 (2011).

605 55. Xu, L. *et al.* Satellite observation of tropical forest seasonality: spatial patterns of

606   carbon exchange in Amazonia. *Environ. Res. Lett.* **10,** 84005 (2015).

607 56. Parazoo, N. C. *et al.* Interpreting seasonal changes in the carbon balance of southern

608   Amazonia using measurements of XCO2 and chlorophyll fluorescence from GOSAT.

609   *Geophys. Res. Lett.* **40,** 2829–2833 (2013).

610 57. Granger, C. W. J. Testing for causality. A personal viewpoint. *J. Econ. Dyn. Control* **2,**

611   329–352 (1980).

612 58. Taylor, K. E., Stouffer, R. J. & Meehl, G. A. An overview of CMIP5 and the

613   experiment design. *Bull. Am. Meteorol. Soc.* **93,** 485–498 (2012).

a Precip → SIF

b SIF → Precip

c PAR → SIF

d SIF → PAR

-1 -0.8 -0.6 -0.4 -0.2 0 0.2 0.4 0.6 0.8 1
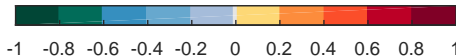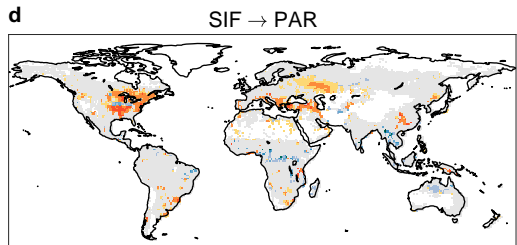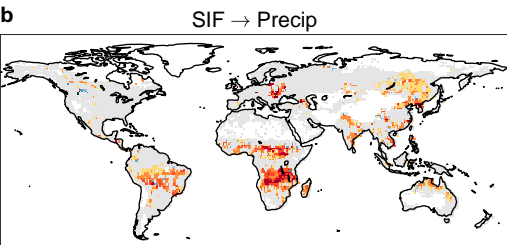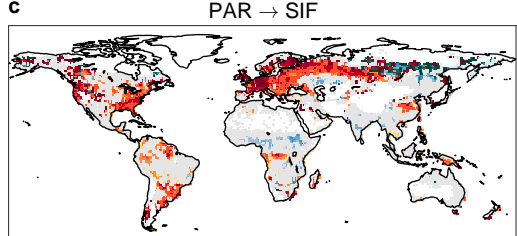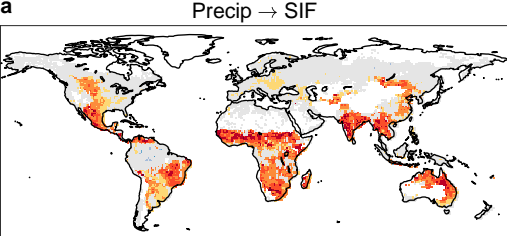
a Precip → SIF → Precip

b PAR → SIF → PAR

-0.3   -0.18   -0.06   0.06   0.18   0.3
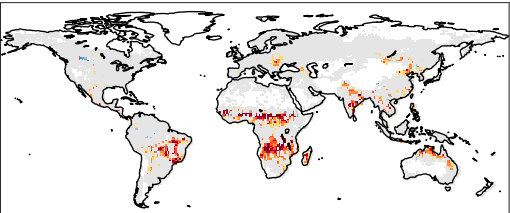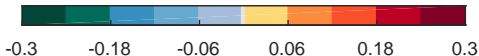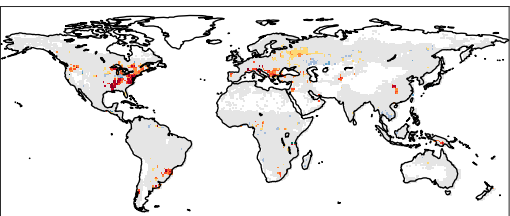
a Precip → Biosphere → Precip **b** PAR → Biosphere → PAR